Multi-dimensional damage measure for seismic reliability analysis

Raffaele De Risi[1], Katsuichiro Goda[2], and Solomon Tesfamariam[3]

[1] Department of Civil Engineering, Queen's Building, University Walk, University of Bristol, BS8 1TR, Bristol, UK; E-mail: raffaele.derisi@bristol.ac.uk

[2] Department of Civil Engineering, Queen's Building, University Walk, University of Bristol, BS8 1TR, Bristol, UK; E-mail: katsu.goda@bristol.ac.uk

[3] School of Engineering, The University of British Columbia, Okanagan Campus, 3333 University Way, V1V 1V7, Kelowna, BC, Canada, E-mail: Solomon.Tesfamariam@ubc.ca

Submitted to:

Structural Safety

Corresponding author:

Raffaele De Risi

E-mai: raffaele.derisi@bristol.ac.uk

Abstract

A new multi-variate approach for assessing the seismic performance of structures is proposed. The classical safety factor formulation in structural reliability is adopted considering multi-dimensional limit state functions that are defined in terms of demand-over-capacity ratios. Variable definitions of multi-dimensional limit state functions represent additional epistemic uncertainty in reliability problems. The use of different multi-dimensional limit state functions is investigated either in terms of variability on the resulting fragility curves and as effect on the risk by calculating the probability of exceeding prescribed limit states. The proposed method is demonstrated by analyzing four non-ductile reinforced concrete structures and by considering bi-dimensional damage measures in terms of maximum inter-story drift and residual drift. Results show that for limit states where the structure behaves elastically, there is no significant effect on the fragility and risk when alternative multi-dimensional measures are adopted. Conversely, average variations up to 10% on the assessment of the probability of failure are observed for limit states where the structure behaves nonlinearly; such variations can be as large as 50% for some particular cases.

Keywords: Multi-dimensional damage measure, Limit state function, Risk assessment, Performance-based earthquake engineering, Incremental dynamic analysis.

1 INTRODUCTION

Seismic reliability methods aim at evaluating the performance of a structure under seismic actions and calculating the probability of attaining (or exceeding) a prescribed set of limit states (Ebrahimian and De Risi, 2014). The probability (P) of attaining a specific limit state (LS) can be expressed as:

$$P_{LS} = P\left[G(\boldsymbol{X}) \leq 0\right] \tag{1}$$

where G is the limit state function or performance function, and $\boldsymbol{X}$ is a set of uncertain parameters of the problem, such as aleatory uncertainties (e.g. earthquake ground motions) and epistemic uncertainties (e.g. material properties and structural details). G defines the boundary between safe and unsafe domains. Such a limit state function is a multi-dimensional surface and is itself uncertain. Its variability can be considered by introducing additional random variables (Hall and Lawry, 2003). With the advancement in computational power, use of surrogate empirical models of the limit state function, e.g., response surface function (RSF) and simulation techniques, is becoming more affordable (Schotanus et al., 2004; Liel et al., 2009; Hadidi et al., 2017). The RSF consists of fitting structural responses, obtained through numerical experiments, by means of a polynomial function in the space of uncertain parameters. Regarding the limit state function, the shape of the RSF can be uncertain (Gupta and Manohar, 2004). Approximations have been proposed for seismic reliability problems (Möller et al., 2009). For high-dimensional reliability analysis (Wang and Song, 2018), for example, an exponential surrogate model may be adopted as alternative to more classical quadratic polynomial functions (Hadidi et al., 2017).

Alternatively, seismic reliability analysis can be carried out by analyzing the entire problem in a modular manner, separating into seismic hazard analysis and structural damage

assessment, and then integrating them all together (Cornell and Krawinkler, 2000). In this case the rate of exceeding a given limit state is obtained as:

$$\lambda_{LS} = \int P[D > C \mid IM] \cdot \left| d\lambda(IM) \right| \tag{2}$$

where D is the structural demand and C is the capacity, both of which are expressed in terms of a predefined set of engineering demand parameters *EDPs*, such as chord rotation or roof drift, describing the mechanical behavior of the structure. *IM* denotes the intensity measure, e.g., peak ground acceleration (*PGA*) and spectral acceleration (S_a). $\lambda(IM)$ is the seismic hazard curve (Cornell, 1968). $P[D>C|IM]$ is the conditional probability of attaining a given limit state (or the probability of failure) for a given value of *IM* and is also known as fragility curve (Celik and Ellingwood, 2010). Moreover, by adopting the demand-to-capacity ratio $Y = D/C$ (Jalayer et al., 2007), Equation 2 can be rewritten as:

$$\lambda_{LS} = \int P[Y > 1 \mid IM] \cdot \left| d\lambda(IM) \right| \tag{3}$$

In the above formulations, the main focus of the reliability problems is to perform the seismic damage assessment in terms of D - C or D/C (= Y).

There are two main concerns in developing seismic fragilities curves. First, the adoption of a single scalar Y may be insufficient (Ataei and Padgett, 2013). For example, Cimellaro and Reinhorn (2010) proposed a multi-variate approach for describing the vulnerable behavior of non-structural components that are sensitive to multiple parameters, such as displacements and accelerations (e.g., partition walls, service systems, etc.). Tesfamariam and Goda (2015) presented a case of maximum and residual inter-story drift ratios for non-ductile RC structures to develop a bi-variate framework for seismic performance assessment for the case of mainshock-aftershock earthquake sequences. Hariri-Ardebili and Saouma (2017) suggested to perform multiple-EDP incremental dynamic analysis (IDA, Vamvatsikos and Cornell, 2004),

when *EDP*s of interest are strongly correlated. Although they suggested the necessity of a multiple-*EDP* IDA, they did not provide details as to how to evaluate the attainment of the limit state, i.e. the definition of the limit state surface. Zenter (2017) also proposed a general framework for the estimation of analytical fragility functions based on multivariate probabilistic distributions. Moreover, Bakalis and Vamvatsikos (2018) presented a short discussion about the need for multiple-EDPs limit states. In addition, the scalar *Y* formulation can also be inappropriate when the *EDP*s of interest are sensitive to different aspects of seismic excitations (Bradley et al., 2015), e.g., two different *IM*s. In such a case, the adoption of a multi-dimensional limit state surface can help develop simple univariate fragility curves (i.e., fragilities depending on a single *IM*) considering the uncertainty introduced by the insufficiency of the selected *IM* for all *EDP*s of interest.

Second, more than one structural component may contribute to the global structural performance (i.e. the problem is multi-dimensional), and the shape of the function mapping the response of single components to the response of the entire structure is uncertain (Ataei and Padgett, 2013). For example, current building codes, such as Eurocodes (CEN, 2002) and ASCE standards (ASCE/SEI, 2017), provide failure surfaces at element level (e.g. columns and beams), defining failure domains in terms of internal forces for different directions (e.g. biaxial flexure and axial load, Bousias et al. 2002) or different internal stresses (e.g. tensile, shear, and torsional stresses, Lu et al., 1994), and assume that the reliability factor defined at section/element level is applicable to entire structure (ASCE/SEI, 2017; CEN, 2002). Therefore, new potential multi-variate damage measures capable of representing the entire structural performance in a comprehensive fashion are needed.

This paper investigates how the shape of a multi-dimensional limit state function can have influence on the seismic reliability assessment; the shape of the limit state function associated with the multi-variate damage measure is a source of epistemic uncertainty to be

112 considered in a comprehensive seismic reliability analysis. Building upon the work proposed
113 in Jalayer et al. (2007), this work presents a novel IDA-based seismic performance evaluation
114 approach that accounts for multiple *EDP*s caused by major earthquakes. This is achieved by
115 defining a multi-dimensional damage measure $\boldsymbol{Y} = [Y_1, Y_2, \ldots, Y_N]$, and corresponding multi-
116 dimensional limit state function $G(\boldsymbol{Y}, IM)$. The limit state function can assume different
117 analytical forms leading to different estimations of the probability of failure. The main output
118 of IDA results in different fragilities functions for each limit state function. Such fragilities,
119 integrated with the same hazard curve (according to Eq. 3), can lead to different failure
120 probabilities. The scope of this work is not to assess which functional form is the best, but to
121 show the influence of the functional form on the probability of failure. The former can be
122 investigated only through experimental or theoretical/numerical studies, which is beyond the
123 scope of this study. Although this study is focused upon the IDA, the proposed approach can
124 be used also for pushover analyses (Krawinkler, 1996) and can be adapted to cloud analysis
125 (Jalayer et al., 2015) and multiple stripe analysis (Baker, 2015) using the approach proposed
126 by Zenter (2017). To demonstrate the proposed procedure, 2-story, 4-story, 8-story, and 12-
127 story RC frame structures described in Tesfamariam and Goda (2015) are adopted as a case
128 study and the maximum and residual drifts due to earthquakes are investigated by means of
129 IDA using a set of 50 ground-motion records. Fragilities obtained considering different limit
130 state surfaces are then convoluted with the seismic hazard for the considered case study area,
131 and the variability in the failure probability in relation to the assumed shape of the failure
132 domain is evaluated.
133
134 ## 2 METHODOLOGY
135 ### 2.1 Multi-dimensional limit state function
136 A multi-dimensional limit state function $G(\boldsymbol{Y}, IM)$ that considers more than one mechanism,
137 and therefore more than one ratio ($Y_i = D_i/C_i$), can be defined as a non-linear combination of Y_i

(Equation 4) or as union or intersection of multiple limit state functions (Equations 5) (Melchers and Beck, 2018):

$$G(\boldsymbol{Y}, IM) = \sum_{i=1}^{N} a_i \cdot Y_i^b - 1 \quad with\ a_i = 1\ or\ 0 \tag{4}$$

$$G(\boldsymbol{Y}, IM) = \bigcup_{j=1}^{N} (G_j \leq 0) \qquad G(\boldsymbol{Y}, IM) = \bigcap_{j=1}^{N} (G_j \leq 0) \tag{5}$$

Equation 5 is a generic expression that can be reduced to a one-dimensional linear limit that is adopted in Jalayer et al. (2007). The presented limit state functions are considered constant with *IM*, therefore this term is dropped in the following for simplicity. Varying the power term *b* in Equation 4 it is possible to obtain different shapes of the limit state function, however, in this paper, only values of *b* greater than or equal to 1 are investigated.

Figure 1 shows the limit state surfaces, at structural level, for the case of two *EDP*s, which is mainly focused in this research. In this study, different limit state surfaces are considered: linear (Fig. 1a), convex-circular (Fig. 1b), convex-square function (Fig. 1c), and concave surface (Fig. 1d). The four shapes for the limit state functions are selected in order to represent a broad spectrum of possible functions and therefore to achieve potential significant variations in the reliability assessment. Such different limit states will depend on the structural typology (e.g., RC and steel) or will be affected by the construction technique (e.g. moment resistant frame and braced frame). For example, the square limit state function (Fig. 1c) represents the conventional safety check performed to design new structures or assess existing ones, i.e., the more restrictive failure mechanism rules the design/assessment. The linear and circular limit state functions (Fig. 1a,b) also have a precise physical meaning: none of the considered EDPs reach its own limit value, but their combination is severe enough to lead to the global failure. This is the case, for example, of global frame instability, i.e. the global

158 collapse is attained before the capacity of each structural element is reached, that is typical of
159 tall steel frame buildings (Gerasimidis et al., 2017). Finally, the concave limit state surface may
160 be applicable to a failure mechanism that requires an entire group of elements to fail; this is the
161 case of the soft-story mechanism, i.e., all top and bottom sections of the columns of a story
162 need to yield (Jalayer et al., 2007). The union and intersection of limit state functions are typical
163 of reliability problems of series and parallel systems, respectively (Ebrahimian and De Risi,
164 2014).

165 The definition of the appropriate limit state function requires data either (1) from field
166 surveys after an earthquake or (2) from laboratory tests (Cimellaro and Reinhorn, 2010). Data
167 can be interpreted based on statistical analysis or engineering judgement. These functions can
168 be also continuously updated in a Bayesian framework when more data are available (Gardoni
169 et al., 2002).

170 With reference to the four limit state functions adopted herein, the linear limit state
171 function shown in Fig. 1a is obtained for $N = 2$, $b = 1$, and $a_i = 1$:

$$G(\boldsymbol{Y}) = Y_1 + Y_2 - 1 \tag{6}$$

172 The circular limit state function shown in Fig. 1b is obtained for $N = 2$, $b = 2$, and $a_i = 1$:

$$G(\boldsymbol{Y}) = Y_1^2 + Y_2^2 - 1 \tag{7}$$

173 Finally, the square and concave surfaces, shown in Figs. 1c and 1d, are obtained as union and
174 intersection of linear limit state surfaces, respectively, imposing $N = 2$, $b = 1$, and $a_1 = 1$ and
175 $a_2 = 0$ (i.e., $G_1(\boldsymbol{Y}) = Y_1 - 1$), and $a_1 = 0$ and $a_2 = 1$ (i.e., $G_2(\boldsymbol{Y}) = Y_2 - 1$), respectively. It is
176 interesting to note that passing from the linear to the square function there is a progressive
177 reduction of dependence between *Ys*. The square function represents the case of independent
178 *Ys* (Cimellaro and Reinhorn, 2010).

179

2.2 IDA-based procedure

The adoption of incremental loading for reliability analysis is an established procedure (Wu and Moan, 1991). The focus is to evaluate values of critical *IM*s (illustrated as red crosses in Fig. 1) corresponding to the passage from the safe to the unsafe domain of the multiple-*EDP* plane (i.e. from the green to red area in Fig. 1). The IDA procedure is considered since it can identify such critical points, i.e., the points on the limit state surface. IDA is similar to the classical *first excursion* or *first passage* problem in reliability theory (Au and Beck, 2001). Therefore, the proposed methodology can be extended to other classical reliability problems involving a multi-dimensional limit state surface.

With IDA, the structural capacity is estimated by repeatedly scaling a ground motion record until a specific damage on the structure is attained. The scaling process leads to the definition of a curve, also known as IDA curve (Fig. 1), that relates increasing *IM* values with structural demand parameters *EDPs* or alternatively damage measures $\boldsymbol{Y}$. The onset of a specific limit state can be identified as the *IM* value for which the demand is greater or equal to the capacity. By repeating this process for a set of ground motions, a set of IDA curves is obtained and therefore a set of *IM* values corresponding to the onset of a specific limit state can be determined. Eventually, the probability of attaining a specific limit state can be estimated; for example, the lognormal distribution is often fitted to the empirical distribution of critical values of *IM*:

$$P[G(\boldsymbol{Y}) \leq 0 | IM] = \Phi\left(\frac{lnIM - ln\eta_{IM}}{\beta_{IM}}\right) \tag{8}$$

where η_{IM} and β_{IM} are, respectively, the median and the logarithmic standard deviation of the intensity measures leading to the overreaching of a given limit state.

For the case of a multi-dimensional limit state surface, the calculation of *IM* values corresponding to the onset of a specific limit state is not straightforward. In fact, it will be

improbable that one of the points of the IDA curve belongs to the limit state surface (i.e., $G = 0$). Therefore, it is necessary to obtain the performance point (i.e., $G = 0$). Practically, this can be done by identifying the first point outside the domain (i.e., $G(\boldsymbol{Y}) < 0$) and the previous one, and then by interpolating these two points at $G(\boldsymbol{Y}) = 0$. Appendixes A and B provide more details on how to calculate the intersection between the line passing through the two points and the multi-dimensional planar and circular limit state surface, respectively.

2.3 Reliability assessment

The closer the limit state surface is to the origin, the lower the critical *IM*s are and therefore, the fragility is more conservative (i.e., for the same probability value, the fragility associated with the linear limit state function provides capacity values smaller than that provided by the fragility associated with the convex limit state function). On the contrary, the farther the limit state surface is from the origin, the larger the structural capacity is for the same probability value. Therefore, passing from the linear limit state function (Fig. 1a) to the concave limit state function (Fig. 1b), it is expected that vulnerability models lead to lower values of risk. For each limit state function, a set of critical points is identified and therefore a fragility curve can be computed using Equation 8.

Figure 2 shows a schematic representation of the four fragility curves corresponding to the four domains examined herein. In the same figure, a typical shape of a seismic hazard curve (magenta line) is also included. Integrating the four fragility curves with the same hazard curve, according to Equation 2, will lead to four different estimations of rate λ_{LS} and, therefore, to four estimations of probability of attaining a specific limit state. In this study, to transform the rate into probability, an observation time window (t) of fifty years is considered and the Poisson distribution is assumed as an underlying probability model (Der Kiureghian, 2005):

$$P_F = 1 - \exp(-\lambda_{LS} \cdot t) \quad (11)$$

In the following the variability of the probability of failure will be investigated as a result of the different limit state function shapes.

In Figure 2, two additional fragility curves are included: the central estimate fragility (dashed black line) and the equivalent fragility (continuous black line). The central estimate is the median curve of the four fragility curves corresponding to the four shapes of the limit state function. On the other hand, the equivalent fragility curve is obtained according to the *mean estimate* approach (Cornell et al., 2002) and therefore it has the same median value of the central estimate fragility and a logarithmic standard deviation (β) equal to:

$$\beta = \sqrt{\left[\frac{1}{2} log\left(\frac{im_{84^{th}}}{im_{16^{th}}}\right)\right]^2 + \left[\frac{1}{2} log\left(\frac{im_+}{im_-}\right)\right]^2} \quad (12)$$

that is the sum of the square of the logarithmic standard deviation of the central estimate fragility and the uncertainty associated with the median estimation. Such a kind of fragility considers the variability of the shape of the limit state surface (i.e., Linear, Circular, Square, Convex) and for this reason has been defined as equivalent. This definition of fragility is physically appropriate since it contains three information: 1) the central median value, 2) the central logarithmic standard deviation and 3) the uncertainty on the shape of the limit state function. The probability of failure will be calculated using this equivalent fragility curve and results will be compared with those obtained using the fragilities having different shapes of the limit state function.

3 CASE STUDY

3.1 Structural models and performance criteria

Archetypical non-ductile RC frame structures, with four different story numbers (2-, 4-, 8- and 12-story), located in Victoria, British Columbia (BC), Canada, are considered as a case study. The structures were designed as a space moment resisting frame, considering all columns and beams part of the lateral resisting system according to the 1967 UBC seismic provisions (ICBO, 1967). Beam and column elements have the same amount of over-strength; each element is 15% stronger than the code-minimum design level. The design is governed by strength and stiffness requirements, as the 1967 UBC had few requirements for special seismic design or ductile detailing.

Figure 3a shows a schematic representation of the 4-story building. It has a floor area of about 2000 m^2; columns are spaced at 7.6 m, and story heights are 4.6 m and 4.0 m at the ground floor and higher floor levels, respectively. The non-ductile RC models used in this paper are developed by Liel and Deierlein (2008). The models are based on a lumped plasticity concept and are implemented in OpenSees (McKenna, 2011). Plastic hinges are modeled as tri-linear nonlinear springs according to Ibarra et al. (2005) model, which is calibrated with data from 255 RC column test results. Figure 3b shows the tri-linear backbone curve, coupled with the associated hysteretic rules, which is used to model the structures to post-peak response and near-collapse response. The post-peak response considers the strain hardening behavior associated with concrete crushing, rebar buckling and fracture, and bond failure (Liel and Deierlein, 2008; Haselton et al., 2008). The first vibration periods (T_1) for the 2-, 4-, 8-, and 12-story buildings are 1.10 s, 1.92 s, 2.23 s, and 2.35 s, respectively.

The seismic performance of a structure is generally evaluated through the maximum inter-story drift ratio (maxISDR). Tesfamariam and Goda (2015) highlighted that, based on recent post-earthquake functionality assessment of structures, the residual inter-story drift ratio

(resISDR) is an important factor for the post-earthquake safety of a building and for the economic feasibility of repair and reconstruction. Similar conclusions were also found by Ramirez and Miranda (2012). Moreover, they demonstrated that maxISDR and resISDR of a MDOF system are statistically dependent, and that their marginal distributions can be represented by the Frechet and generalized Pareto distributions, respectively, whereas their dependence can be characterized by the asymmetrical Gumbel copula (Nelsen, 2007).

Table 1 summarizes the limits of maxISDR and resISDR for IO, DC, LS and CP; maxISDR limit values are obtained combining the values in Table 6-8 of the FEMA 356 (2000) with the experimental values reported in the FEMA P-58 supplementary (2009). resISDR limit values are based on Table C-1 of the FEMA P-58-1 (2012). The resISDR limits for CP are expressed in terms of the design shear force V_{design} normalized by the building weight W to consider cases where P-delta might be dominant at smaller drift ratios.

3.3 Seismic hazard and ground motion selection

Victoria is the provincial capital of BC and is located at the southern tip of Vancouver Island. Atkinson and Goda (2011) conducted seismic hazard studies for southwestern BC, by incorporating recent advancements in seismology. Typical outputs from probabilistic seismic hazard analysis, which are essential for seismic performance assessment of buildings and infrastructure, are the seismic hazard curves, from which uniform hazard spectra (UHS) and seismic disaggregation are obtained. Figure 4a shows seismic hazard curves for Victoria for spectral acceleration varying from the PGA to $S_a(T_1 = 3s)$ and for site class C, which is represented by the average shear-wave velocity in the upper 30 m between 360 m/s and 760 m/s. Figure 4b shows the corresponding UHS for Victoria at 10% and 2% probability of exceedance (PE) in 50 years. Currently, the UHS at 2% PE in 50 years (equivalent to the return

297 period of 2475 years) is adopted as the basis for seismic design provisions for new construction
298 in Canada.

299 For ground motion record selection to be used in IDA, the multiple conditional mean
300 spectrum (CMS) method proposed by Goda and Atkinson (2011) is adopted to define the target
301 response spectra. The multiple CMS, based on the deaggregation results, allows to select an
302 adequate set of ground motion records considering relative seismic hazard contributions from
303 different earthquake sources (i.e. crustal events, interface events, and inslab events) in
304 subduction zones. A set of 50 records (selected from the NGA, K-NET, KiK-net, and SK-net)
305 are selected to carry out the IDA. The spectral acceleration at the fundamental period of the
306 structure is used as reference intensity measure. More specifically, for the 2-story building, the
307 spectral acceleration at 1.0 s is selected, and the scaling range in IDA is varied from 0.05 g to
308 1.4 g, while for the 4-, 8-, and 12-story buildings, the spectral acceleration at 2.0 s is used and
309 it ranges between 0.05 g and 0.7 g. For the risk assessment, the hazard curves of the spectral
310 acceleration corresponding to 1.0 s and 2.0 s are adopted for the case of the 2-story building
311 and 4-, 8-, and 12-story buildings, respectively. There are two practical reasons in adopting
312 only 1.0 s and 2.0 s: (a) Canadian hazard values are only available at 1 s and 2 s, and (b)
313 considering a common period for 4, 8 and 12 stories facilitated the direct comparison of IDA
314 results.

315

316 ## 4 RESULTS

317 ### 4.1 IDA results

318 Figure 5 shows the 3D representation of the IDAs for the 4-story building in the space of
319 maxISDR and resISDR. On the same curves, the critical points corresponding to different limit
320 states are also indicated. It is possible to observe that for the linear (Fig. 5a), circular (Fig. 5b),
321 and square (Fig. 5c) cases, the points are grouped in regular clouds well separated each other,

while for the concave case (Fig. 5d), the points are more dispersed, and the clouds are more overlapped. This is because the limit state surface cuts all the IDA curves in the region of high nonlinearity of the structure.

Figure 6 shows the two-dimensional view of the same IDAs but in the plane Y_1-Y_2 where Y_1 is the ratio between the maximum demand ISDR ($maxISDR_D$) and the associated capacity ($maxISDR_C$) according to Table 1, and Y_2 is the ratio between the residual ISDR ($resISDR_D$) and the associated capacity ($resISDR_C$). Moreover, different limit states and different limit state surfaces are shown. Although these results are shown for the 4-story building only, the following comments are generally applicable to the other three cases (i.e. 2-, 8-, and 12-story structures). The results for the 2-, 8-, and 12-story structures are included in the tables. It is possible to observe that for the cases of IO (Figs. 6a-d) and DC (Figs. 6e-h), the concave functions lead to critical points in the nonlinear part of the IDA, contradicting the physical descriptions of IO and DC. Therefore, in the following these two cases will be neglected. It is also worth noting that passing from IO to CP there is a larger part of the limit state surface intersected by the IDA curves, leading to a larger dispersion of the response. Moreover, for the case of the square limit state functions (i.e. Figs. 6c,g,f,p), the proposed procedure is almost coincident with the classic procedure adopted for the case of scalar damage measure; therefore, in Section 4.3, risk values obtained with the square limit state surface will be adopted as reference case.

4.2 Fragilities

Figure 7 shows the fragility curves obtained for the four limit states and for different limit state functions. As emphasized before, the concave limit state function leads to the unrealistic fragility curves (blue lines in Figs. 7a-b) for the case of IO and DC, therefore such fragilities are disregarded. More in general, it is possible to observe that for IO and DC, fragilities

obtained for different limit state functions are coincident, as also evident from the statistics listed in Table 2. More variability between fragilities obtained for different limit state functions can be appreciated for the cases of LS and CP (Figs. 7c-d). For the latter two limit states passing from the linear to the concave function, there is an increase of both median and logarithmic standard deviation. Especially for the case of LS, an overall variation of about 50% on the median and about 40% on the logarithmic standard deviation can be observed (Table 2). Analogously, for the case of CP, variation of about 20% on the median and about 40% on the logarithmic standard deviation are observed (Table 2).

Figure 7 also shows the equivalent fragilities obtained according to Section 2.3, and their statistics are listed in Table 3. They differ from the fragilities presented in the first row of Fig. 7 for the case of LS and CP. On the contrary, they are almost coincident with the fragilities obtained for IO and DC. In any case, the equivalent fragility tends to coincide with the fragility obtained with the square function.

4.3 Reliability assessment

The probability of attaining a prescribed limit state is calculated according to Section 2.3. Fig. 8a shows the probability of failure for the four limit states and for the fragility models obtained according to the different limit state surfaces. The risk calculated with the equivalent fragility model is also presented. First, the probability of failure decreases passing from IO to CP (Table 4). Second, as direct consequence of the fragility shapes, no significant variation of probability of failure can be observed among the five different fragility models for the case of IO and LS. In contrast, greater variability is observed for the cases of LS and CP. The risk assessment based on the equivalent fragility model is a sort of average assessment of the risk values obtained considering the four different fragilities based on different limit state functions.

As mentioned in Section 4.1, the risk value corresponding to the square limit state function can be used as a reference. Figure 8b shows the probability of failure, normalized with respect to that of the square limit state function. It is possible to observe that, varying the limit state function, significant variation can occur (up to 50%) for LS and CP. Considering the equivalent fragility only, it is possible to observe that a variation between 3% and 8% of the probability of failure for LS and CP can occur. For the examined case, the variability in the limit state surface leads to a potential error in the risk assessment on average less than 10%. Therefore, the additional uncertainty due to the shape of the limit state function should be considered when the main contribution to the risk is due to the non-linear behavior of the structure.

5 SUMMARY AND CONCLUSIONS

This paper presented a new procedure to define multi-dimensional limit state functions based on non-linear combination of demand-over-capacity ratios or as union/intersection of simple limit state functions. Such multi-dimensional limit state functions are particularly relevant when several *EDP*s need to be considered to assess the performance of a structural system. This is the case of *EDP*s strongly correlated, not all well predicted by the same *IM*, or due to multi-hazard actions. The effects of different limit state functions were investigated both in terms of fragility curve variability and risk assessment. The proposed procedure was specialized for the case of IDA but can still be generalized for other analysis procedures. Analytical methods of identifying the performance points on the limit state functions were also provided (Appendices A and B).

As a case study, four reinforced concrete structures, typical of the Canadian construction, were investigated; more specifically a 2-, 4-, 8-, and 12-story structures were analyzed. The results indicated that for limit states for which the structure behaves elastically,

there is no significant effect due to the different definitions of the limit state functions on the fragility and risk. On the other hand, variations up to 50% on the assessment of the probability of failure were observed for limit states for which the structure behaves nonlinearly for different limit state functions. Accounting for the variability of the limit state function via equivalent fragility curves leads to an average variation of the risk assessment to up to 10%.

Future research should consider more sophisticated case studies, focusing on structural systems with more than two *EDP*s or with different non-linear combinations of the basic limit state surfaces.

ACKNOWLEDGEMENTS

The research is funded by the Engineering and Physical Sciences Research Council (EPSRC) grant (EP/M001067/1) for the first author, the Leverhulme Trust (RPG-2017-006, GENESIS project) for the second author, and Natural Sciences an Engineering Research Council of Canada (RGPIN-2014-05013) under the Discovery Grant programs for the third author.

REFERENCES

ASCE/SEI (ASCE/Structural Engineering Institute). (2017). Minimum design loads for buildings and other structures. ASCE/SEI 7-16, Reston, VA.

Ataei, N., & Padgett, J. E. (2013). Limit state capacities for global performance assessment of bridges exposed to hurricane surge and wave. Structural Safety, 41, 73–81.

Atkinson, G.M., & Goda, K. (2011). Effects of seismicity models and new ground motion prediction equations on seismic hazard assessment for four Canadian cities. Bulletin of the Seismological Society of America. 101, 176–189.

Au, S. K., & Beck, J. L. (2001). First excursion probabilities for linear systems by very efficient importance sampling. Probabilistic Engineering Mechanics, 16(3), 193–207.

421 Bakalis, K., & Vamvatsikos, D. (2018). Seismic Fragility Functions via Nonlinear Response
422 History Analysis. Journal of Structural Engineering, 144(10), 04018181.
423 Baker, J. W. (2015). Efficient analytical fragility function fitting using dynamic structural
424 analysis. Earthquake Spectra, 31(1), 579–599.
425 Bousias, S. N., Panagiotakos, T. B., & Fardis, M. N. (2002). Modelling of RC members under
426 cyclic biaxial flexure and axial force. Journal of Earthquake Engineering, 6(02), 213–238.
427 Bradley, B. A., Burks, L. S., & Baker, J. W. (2015). Ground motion selection for simulation-
428 based seismic hazard and structural reliability assessment. Earthquake Engineering &
429 Structural Dynamics, 44(13), 2321–2340.
430 Celik, O. C., & Ellingwood, B. R. (2010). Seismic fragilities for non-ductile reinforced
431 concrete frames–Role of aleatoric and epistemic uncertainties. Structural Safety, 32(1), 1–
432 12.
433 CEN (2002). European Committee for Standardization, Eurocode 0 – Basis of structural design,
434 EN 1990.
435 Cimellaro, G. P., & Reinhorn, A. M. (2010). Multidimensional performance limit state for
436 hazard fragility functions. Journal of Engineering Mechanics, 137(1), 47–60.
437 Cornell, C. A. (1968). Engineering seismic risk analysis. Bulletin of the Seismological Society
438 of America, 58(5), 1583–1606.
439 Cornell, C.A., & Krawinkler, H. (2000). Progress and challenges in seismic performance
440 assessment. PEER Center News 3(2):1-3. http://peer.berkeley.edu/news/2000spring
441 /performance.html.
442 Cornell, C. A., Jalayer, F., Hamburger, R. O., & Foutch, D. A. (2002). Probabilistic basis for
443 2000 SAC federal emergency management agency steel moment frame guidelines. Journal
444 of Structural Engineering, 128(4), 526–533.

445 Der Kiureghian, A. (2005). Non-ergodicity and PEER's framework formula. Earthquake
446 Engineering & Structural Dynamics, 34(13), 1643–1652.
447 Ebrahimian, H., & De Risi, R. (2014). Seismic reliability assessment, alternative methods for.
448 Encyclopedia of Earthquake Engineering, 1-29. Doi: 10.1007/978-3-642-36197-5_245-1.
449 FEMA 356 (2000). Prestandard and Commentary for the Seismic Rehabilitation of Buildings.
450 Federal Emergency Management Agency, Washington, D.C.
451 FEMA P-58/BD-3.8.6 (2009). Fragility Functions for Reinforced Concrete Moment Frames –
452 Background Document. Federal Emergency Management Agency, Washington, D.C.
453 FEMA P-58-1 (2012). Seismic Performance Assessment of Buildings Volume 1 –
454 Methodology. Federal Emergency Management Agency, Washington, D.C.
455 Gardoni, P., Der Kiureghian, A., & Mosalam, K. M. (2002). Probabilistic capacity models and
456 fragility estimates for reinforced concrete columns based on experimental observations.
457 Journal of Engineering Mechanics, 128(10), 1024-1038.
458 Gerasimidis, S., Deodatis, G., Yan, Y., & Ettouney, M. (2017). Global instability induced
459 failure of tall steel moment frame buildings. Journal of Performance of Constructed
460 Facilities, 31(2), 04016082.
461 Goda, K., & Atkinson, G. M. (2011). Seismic performance of wood-frame houses in south-
462 western British Columbia. Earthquake Engineering & Structural Dynamics, 40(8), 903–924.
463 Gupta, S., & Manohar, C. S. (2004). An improved response surface method for the
464 determination of failure probability and importance measures. Structural Safety, 26(2), 123–
465 139.
466 Hadidi, A., Azar, B. F., & Rafiee, A. (2017). Efficient response surface method for high-
467 dimensional structural reliability analysis. Structural Safety, 68, 15–27.
468 Hall, J. W., & Lawry, J. (2003). Fuzzy label methods for constructing imprecise limit state
469 functions. Structural Safety, 25(4), 317–341.

Hariri-Ardebili, M. A., & Saouma, V. E. (2017). Single and multi-hazard capacity functions for concrete dams. Soil Dynamics and Earthquake Engineering, 101, 234-249.

Haselton, C.B., Liel, A.B., Lange, S.T., & Deierlein, G.G. (2008). Beam-Column Element Model Calibrated for Predicting Flexural Response Leading to Global Collapse of RC Frame Buildings. PEER Report 2007/03, PEER Center, University of California, Berkeley, Berkeley, CA.

Ibarra, L.F., Medina, R.A. & Krawinkler, H. (2005). Hysteretic models that incorporate strength and stiffness deterioration. Earthquake Engineering & Structural Dynamics, 34, 1489–1511.

ICBO (1967). Uniform Building Code. International Conference of Building Officials, Pasadena, CA.

Jalayer, F., Franchin, P., & Pinto, P. E. (2007). A scalar damage measure for seismic reliability analysis of RC frames. Earthquake Engineering & Structural Dynamics, 36(13), 2059–2079.

Jalayer, F., De Risi, R., & Manfredi, G. (2015). Bayesian Cloud Analysis: efficient structural fragility assessment using linear regression. Bulletin of Earthquake Engineering, 13(4), 1183–1203.

Krawinkler, H. (1996). Pushover analysis: why, how, when, and when not to use it. In Proceedings of the 65th Annual Convention of the Structural Engineers Association of California.

Liel, A.B., & Deierlein, G.G. (2008). Assessing the collapse risk of California's existing reinforced concrete frame structures: metrics for seismic safety decisions. Technical Report No. 166, John A. Blume Center Earthquake Engineering Center, Stanford, CA.

Liel, A. B., Haselton, C. B., Deierlein, G. G., & Baker, J. W. (2009). Incorporating modeling uncertainties in the assessment of seismic collapse risk of buildings. Structural Safety, 31(2), 197–211.

Lu, R., Luo, Y., & Conte, J. P. (1994). Reliability evaluation of reinforced concrete beams. Structural Safety, 14(4), 277–298.

McKenna, F. (2011). OpenSees: a framework for earthquake engineering simulation. Computing in Science & Engineering, 13(4), 58–66.

Melchers, R. E., & Beck, A. T. (2018). Structural reliability analysis and prediction. John Wiley & Sons.

Möller, O., Foschi, R. O., Rubinstein, M., & Quiroz, L. (2009). Seismic structural reliability using different nonlinear dynamic response surface approximations. Structural Safety, 31(5), 432–442.

Nelsen, R. B. (2007). An introduction to copulas. Springer Science & Business Media.

Ramirez, C. M., & Miranda, E. (2012). Significance of residual drifts in building earthquake loss estimation. Earthquake Engineering & Structural Dynamics, 41(11), 1477–1493.

Schotanus, M. I. J., Franchin, P., Lupoi, A., & Pinto, P. E. (2004). Seismic fragility analysis of 3D structures. Structural Safety, 26(4), 421–441.

Tesfamariam, S., & Goda, K. (2015). Seismic performance evaluation framework considering maximum and residual inter-story drift ratios: application to non-code conforming reinforced concrete buildings in Victoria, BC, Canada. Frontiers in Built Environment, 1(18). Doi: https://doi.org/10.3389/fbuil.2015.00018.

Vamvatsikos, D., & Cornell, C. A. (2004). Applied incremental dynamic analysis. Earthquake Spectra, 20(2), 523–553.

Wang, Z., & Song, J. (2018). Hyper-spherical extrapolation method (HEM) for general high dimensional reliability problems. Structural Safety, 72, 65–73.

Wu, Y. L., & Moan, T. (1991). An incremental load formulation for limit states in the reliability analysis of nonlinear systems. Structural Safety, 10(4), 307–325.

519 Zentner, I. (2017). A general framework for the estimation of analytical fragility functions
520 based on multivariate probability distributions. Structural Safety, 64, 54–61
521

522 **Figure captions**

523 **Fig. 1.** Multi-dimensional limit state surface for the case of two *EDP*s: (a) Linear, (b)
524 Circular, (c) Square, and (d) Concave surfaces.

525 **Fig. 2.** Fragility curves corresponding to different limit state surfaces and equivalent
526 fragility curves. A typical hazard curve is shown in magenta.

527 **Fig. 3.** (a) Nonlinear finite-element model of a 4-story non-ductile RC frame, and (b)
528 backbone curve for beam-column elements.

529 **Fig. 4.** (a) Seismic hazard curves, and (b) uniform hazard spectra for CP ad LS.

530 **Fig. 5.** Three-dimensional representation of the IDA curves in terms of maxISDR and
531 resISDR for the four limit state surfaces: (a) Linear, (b) Circular, (c) Square, and
532 (d) Concave. Colored dots represent the critical points.

533 **Fig. 6** Bi-dimensional representation of IDA curves in terms of *Y* for (a-d) IO, (e-h) DC,
534 (i-m) LS, and (n-q) CP, overlaid with the four limit state surfaces considered herein.
535 Colored dots represent the critical points.

536 **Fig. 7.** Fragility curves obtained for the (a) IO, (b) DC, (c) LS, and (d) CP. Equivalent
537 fragility curves obtained for (e) IO, (f) DC, (g) LS, and (h) CP.

538 **Fig. 8.** (a) Probability of failure and (b) normalized probability of failure for different limit
539 states and different limit state surfaces.

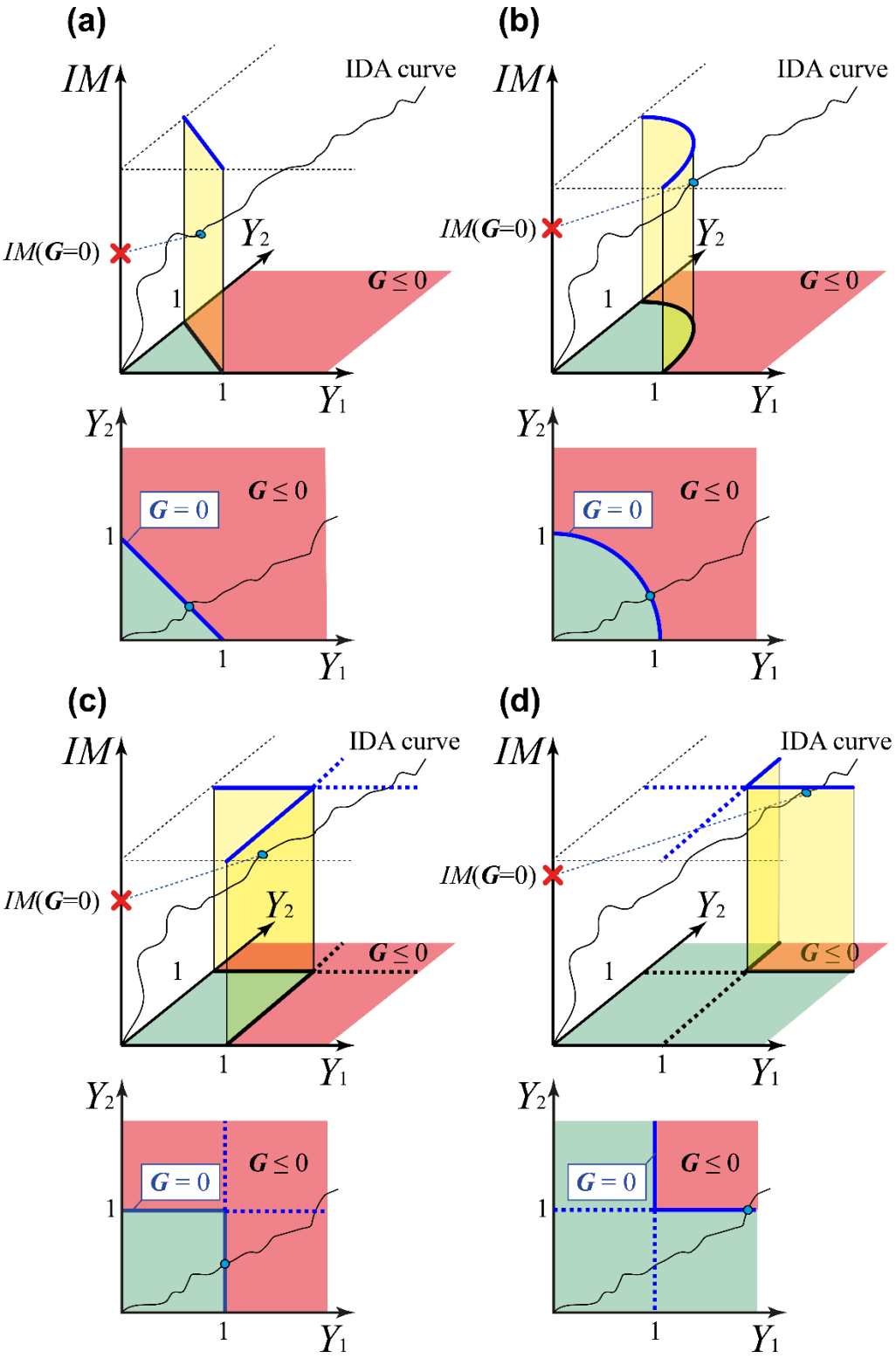

Fig. 1 Multi-dimensional limit state surface for the case of two *EDP*s: (a) Linear, (b) Circular, (c) Square and (d) Concave surfaces.

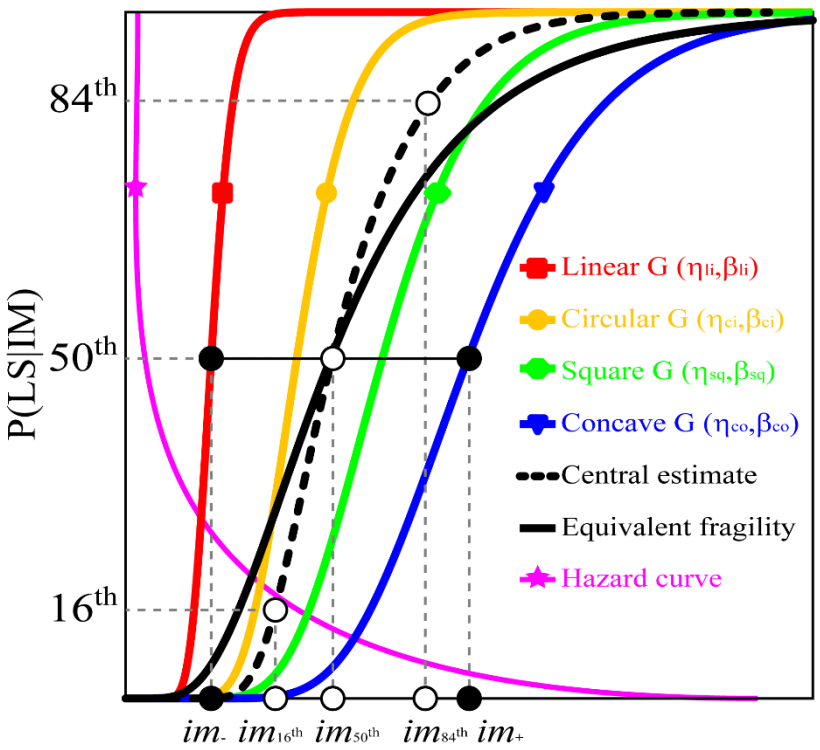

544

545 **Fig. 2** Fragility curves corresponding to different limit state surfaces and equivalent fragility

546 curves. A typical hazard curve is shown in magenta.

547

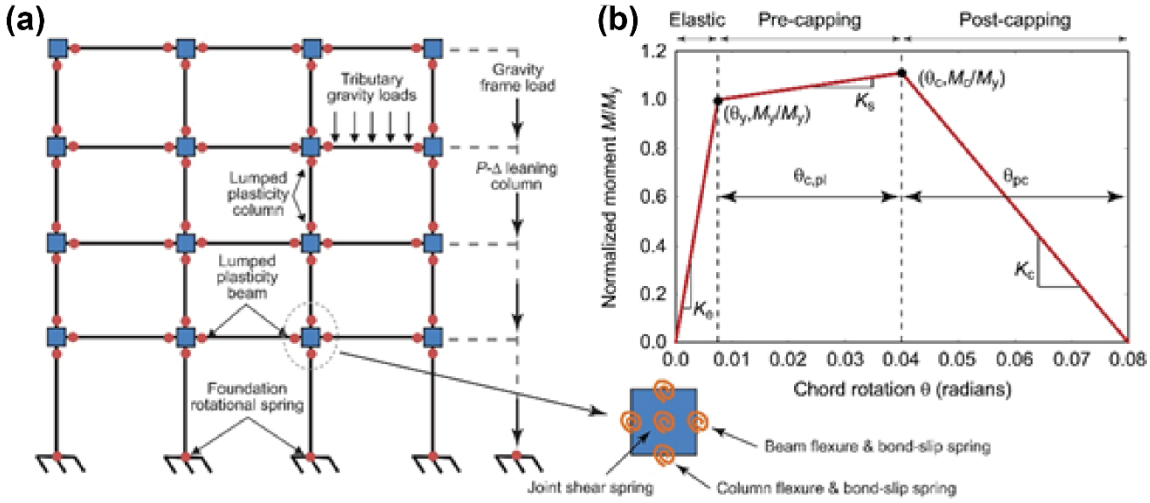

548

549 **Fig. 3** (a) Nonlinear finite-element model of a 4-story non-ductile RC frame, and (b)

550 backbone curve for beam-column elements.

551

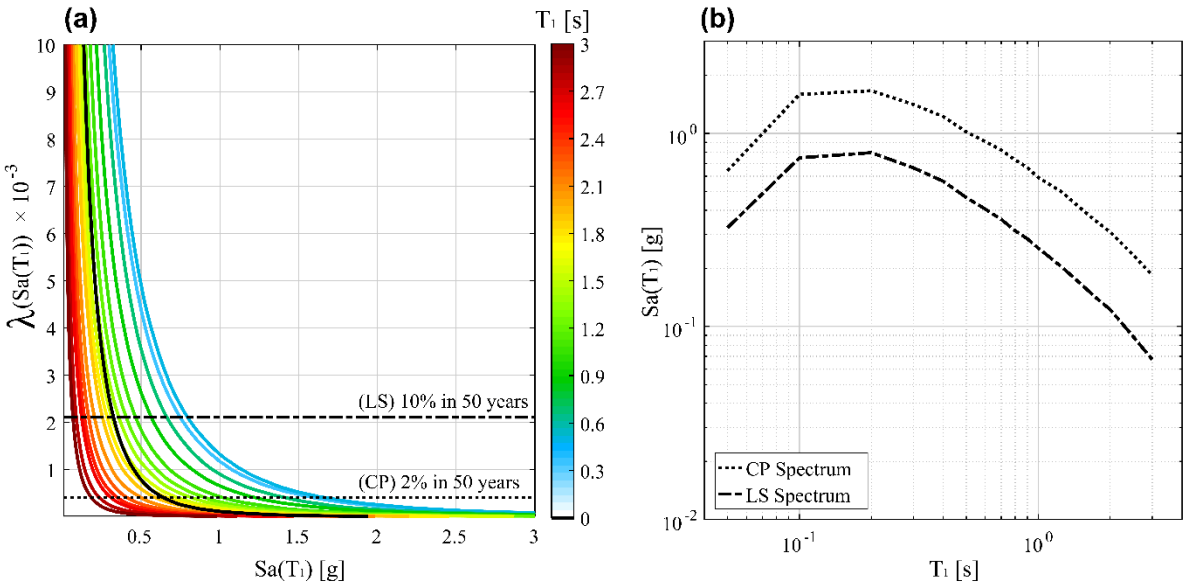

552

553 **Fig. 4** (a) Seismic hazard curves, and (b) uniform hazard spectra for CP ad LS.

554

555

556

557

558

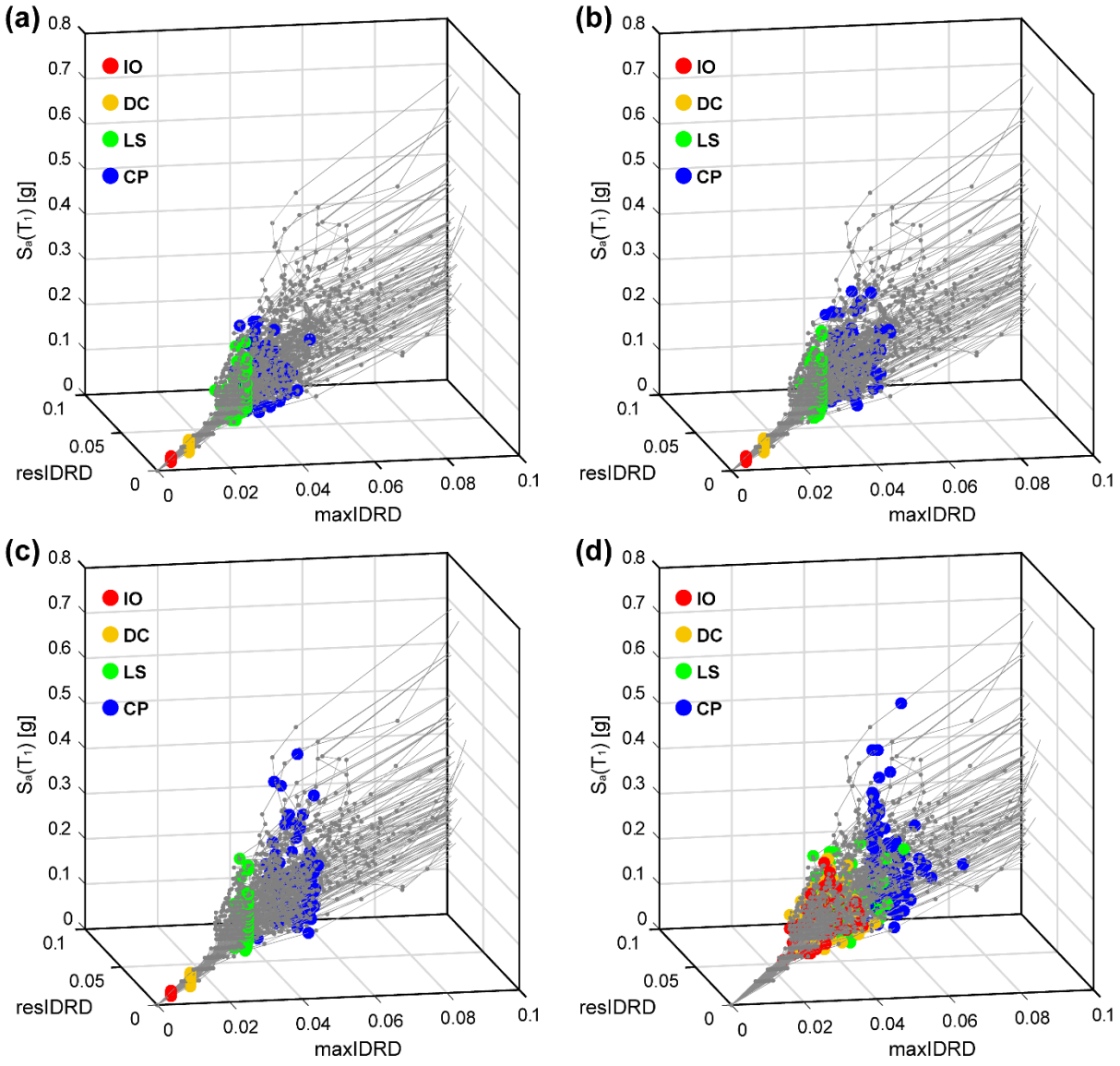

559

560 **Fig. 5** Three-dimensional representation of the IDA curves in terms of maxISDR and resISDR

561 for the four limit state surfaces: (a) Linear, (b) Circular, (c) Square, (d) Concave. Colored dots

562 represent the critical points.

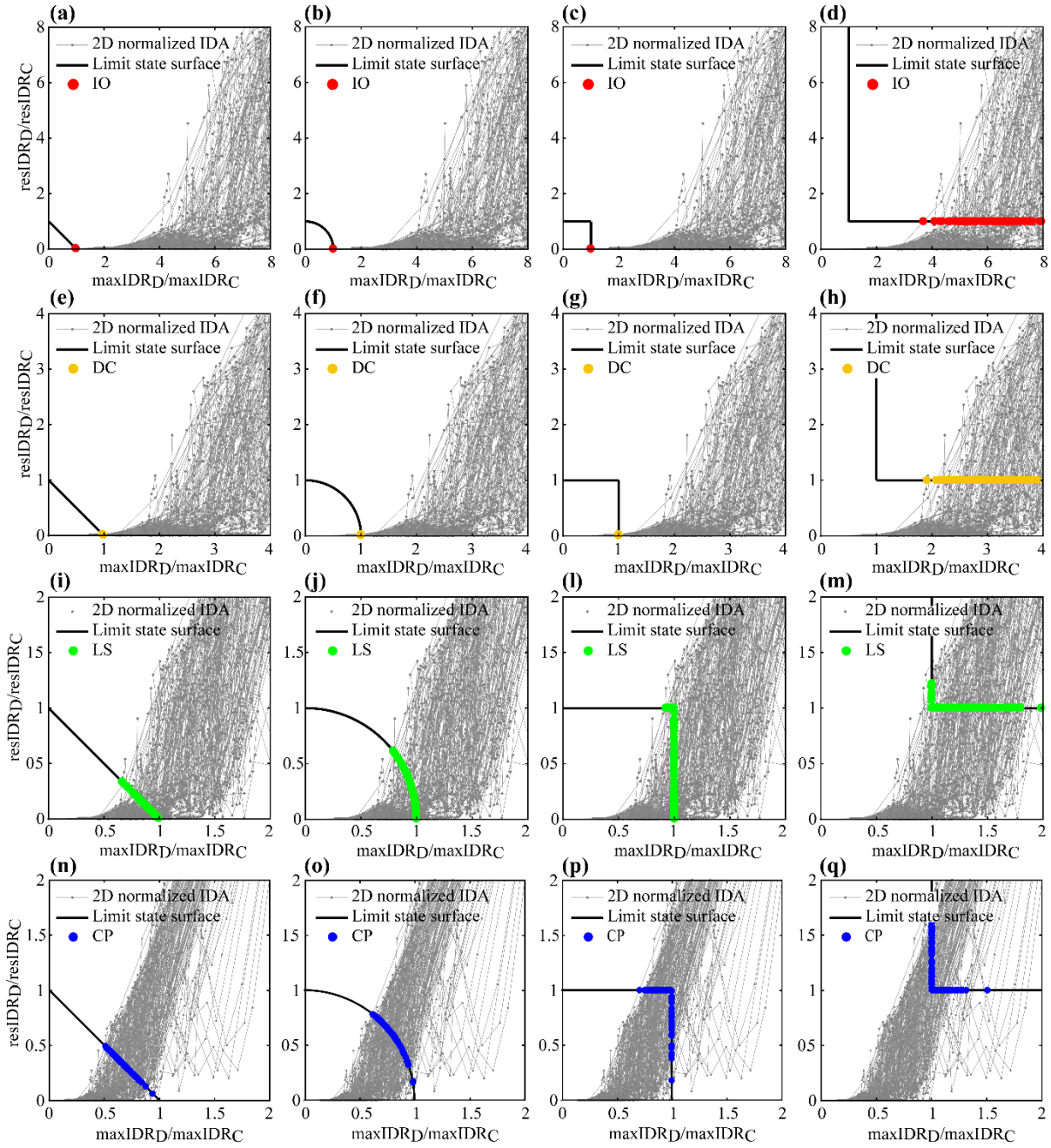

563

564 **Fig. 6** Bi-dimensional representation of IDA curves in terms of ***Y*** for (a-d) IO, (e-h) DC, (i-

565 m) LS, and (n-q) CP, overlaid with the four limit state surfaces considered herein. Colored

566 dots represent the critical points.

567

568

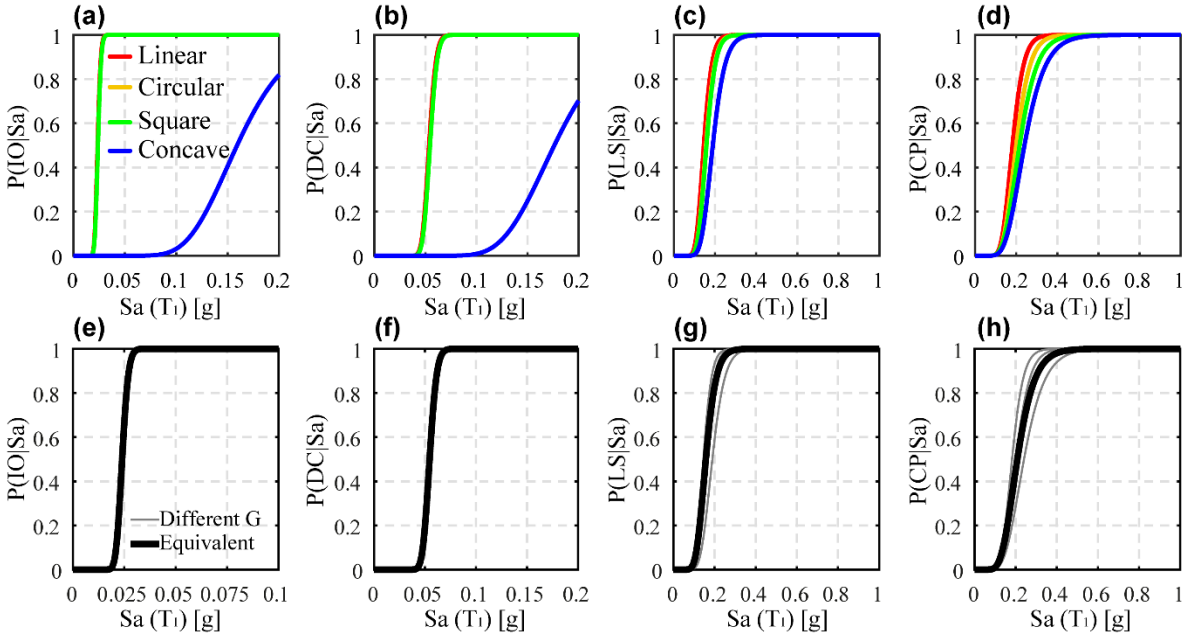

Fig. 7 Fragility curves obtained for the (a) IO, (b) DC, (c) LS, and (d) CP. Equivalent fragility curves obtained for (e) IO, (f) DC, (g) LS, and (h) CP.

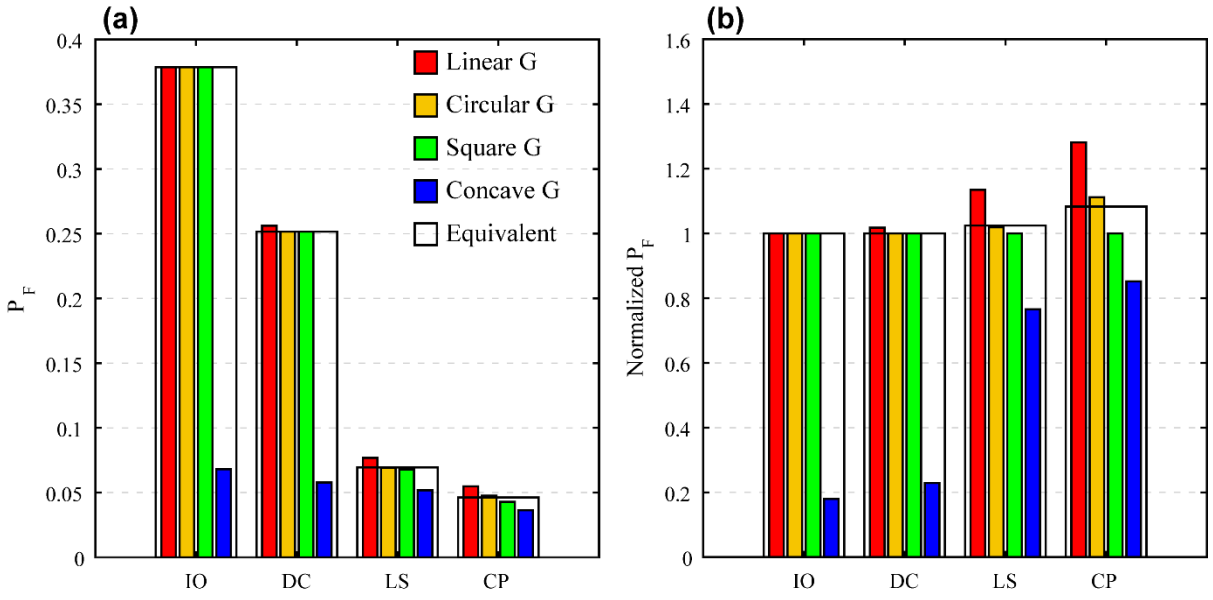

Fig. 8 (a) Probability of failure and (b) normalized probability of failure for different limit states and different limit state surfaces.

Tables

Table 1 Limit states for maximum and residual inter-story drift ratios (FEMA 356, 2000; FEMA P-58-1, 2012). *These numbers are applicable to moderate ductility systems.

Limit State	$maxISDR_C$	$resISDR_C$
IO	0.4%	0.2%
DC	0.9%	0.5%
LS	2.5%	1.0%
CP	4.5%	2.0%*

Table 2 Fragilities statistics for different structural models (**S2**: 2-story, **S4**: 4-story, **S8**: 8-story, **S12**: 12-story), different limit states and different limit state functions (Li = Linear, Ci=Circular, Sq=Square, and Co=Convex).

	IO								**DC**							
	η [g]				**β**				**η [g]**				**β**			
	Li	**Ci**	**Sq**	**Co**	**Li**	**Ci**	**Sq**	**Co**	**Li**	**Ci**	**Sq**	**Co**	**Li**	**Ci**	**Sq**	**Co**
S2	0.07	0.07	0.07	0.29	0.11	0.10	0.10	0.25	0.16	0.17	0.17	0.35	0.17	0.16	0.16	0.29
S4	0.02	0.02	0.02	0.16	0.10	0.10	0.10	0.25	0.05	0.05	0.05	0.18	0.10	0.10	0.10	0.24
S8	0.04	0.04	0.04	0.17	0.21	0.21	0.21	0.32	0.08	0.08	0.08	0.22	0.22	0.22	0.22	0.37
S12	0.05	0.05	0.05	0.21	0.25	0.25	0.25	0.35	0.10	0.11	0.11	0.25	0.25	0.25	0.25	0.38

	LS								**CP**							
	η [g]				**β**				**η [g]**				**β**			
	Li	**Ci**	**Sq**	**Co**	**Li**	**Ci**	**Sq**	**Co**	**Li**	**Ci**	**Sq**	**Co**	**Li**	**Ci**	**Sq**	**Co**
S2	0.32	0.37	0.40	0.42	0.25	0.28	0.33	0.34	0.40	0.44	0.45	0.47	0.34	0.35	0.36	0.37
S4	0.15	0.16	0.16	0.19	0.21	0.21	0.22	0.25	0.18	0.20	0.22	0.24	0.24	0.27	0.30	0.33
S8	0.17	0.20	0.20	0.25	0.30	0.33	0.34	0.41	0.23	0.25	0.26	0.27	0.39	0.42	0.43	0.44
S12	0.21	0.24	0.25	0.27	0.33	0.35	0.36	0.41	0.27	0.28	0.28	0.29	0.40	0.41	0.41	0.41

Table 3 Equivalent fragilities statistics for different structural models (**S2**: 2-story, **S4**: 4-story, **S8**: 8-story, **S12**: 12-story) and different limit states.

	IO		**DC**		**LS**		**CP**	
	η [g]	**β**	**η [g]**	**β**	**η [g]**	**β**	**η [g]**	**β**
S2	0.07	0.10	0.17	0.16	0.38	0.34	0.44	0.36
S4	0.02	0.10	0.05	0.10	0.16	0.25	0.21	0.32
S8	0.04	0.21	0.08	0.22	0.20	0.38	0.25	0.43
S12	0.05	0.25	0.11	0.25	0.24	0.38	0.28	0.41

Table 4 Probability of failure in 50 years for different structures (**S2**: 2-story, **S4**: 4-story, **S8**: 8-story, **S12**: 12-story), different limit state functions and different limit states (Li = Linear, Ci=Circular, Sq=Square, and Co=Convex).

	IO				**DC**			
	Li	**Ci**	**Sq**	**Co**	**Li**	**Ci**	**Sq**	**Co**
S2	38%	38%	38%	8.6%	19%	18%	18%	6.5%
S4	38%	38%	38%	6.8%	26%	25%	25%	5.8%
S8	35%	35%	35%	6.2%	17%	16%	16%	4.4%
S12	28%	28%	28%	4.7%	12%	12%	12%	3.7%

	LS				**CP**			
	Li	**Ci**	**Sq**	**Co**	**Li**	**Ci**	**Sq**	**Co**
S2	7.4%	5.8%	5.2%	4.9%	5.3%	4.5%	4.3%	4.1%
S4	7.7%	6.9%	6.7%	5.2%	5.5%	4.8%	4.3%	3.6%
S8	6.3%	5.1%	5.0%	3.8%	4.2%	3.8%	3.6%	3.3%
S12	4.7%	3.8%	3.5%	3.2%	3.3%	3.1%	3.0%	2.8%

Appendix A

Let **n** ([n_1, n_2, …, n_N]) be the normal vector to the plane representing the limit state surface and **Q** ([q_1, q_2, …, q_N]) a point on the plane. Let **P** ([p_1, p_2, …, p_N]) and **R** ([r_1, r_2, …, r_N]) also be two points inside and outside the failure domain, respectively, associated to two values of spectral acceleration $\mathbf{Sa_P}$ and $\mathbf{Sa_R}$. The direction **l** ([l_1, l_2, …, l_N]) of the line passing by **P** and **R** is:

$$\boldsymbol{l} = \frac{[r1 - p1, r2 - p2, \dots, r_N - p_N]}{\sqrt{(r1 - p1)^2 + (r2 - p2)^2 + \dots + (r_N - p_N)^2}} \quad \text{(A1)}$$

Let be **X** ([x_1, x_2, …, x_N]) the intersection point between the segment linking **P** and **R** and the plane of normal **n**. To **X** is associated an unknown value of spectral acceleration Sa_X that can be calculated as follows.

First, the point **X** can be obtained according the following equation:

$$\boldsymbol{X} = \boldsymbol{P} + d \cdot \boldsymbol{l} \quad \text{(A2)}$$

where *d* is a scalar representing the distance of the segment between **P** and **X** that is obtained as follows:

$$d = \frac{\sum_{i=1}^{N}(q_i - p_i) \cdot n_i}{\sum_{i=1}^{N} l_i \cdot n_i} \quad \text{(A3)}$$

For the specific case of linear limit state surface, **Q** is equal to [1,0, …, 0] and **n** is equal to $\left[1/\sqrt{N}, 1/\sqrt{N}, \dots, 1/\sqrt{N}\right]$. For the cases of square and concave limit states, the N planes defining the domains can be completely described imposing both $\mathbf{Q_j}$ and $\mathbf{n_j}$ to [0,0, …, j^{th} term =1, …, 0] for each j^{th} plan (with j varying between 1 and N).

Finally, once **X** is known, the value of spectral acceleration associated to **X** can be obtained as follows:

$$S_{aX} = S_{aP} + \frac{x1 - p1}{r1 - p1}(S_{aR} - S_{aP}) \cdot \quad \text{(A4)}$$

Appendix B

Let's consider a spherical limit state surface with radius equal to 1 and center in the origin of the axes. Let **P** ([p_1, p_2, …, p_N]) and **R** ([r_1, r_2, …, r_N]) be two points inside and outside the failure domain, respectively, associated to two values of spectral acceleration $\mathbf{Sa_P}$ and $\mathbf{Sa_R}$. The direction **l** ([l_1, l_2, …, l_N]) of the line passing by **P** and **R** is:

$$\boldsymbol{l} = \frac{[r1 - p1, r2 - p2, \dots, r_N - p_N]}{\sqrt{(r1 - p1)^2 + (\,r2 - p2)^2 + \ \dots + (r_N - p_N)^2}} \tag{B1}$$

Let be **X** ([x_1, x_2, …, x_N]) the intersection point between the segment linking **P** and **R** and the sphere. To **X** is associated an unknown value of spectral acceleration Sa_X that can be calculated as follows.

First, the point **X** can be obtained according the following equation:

$$\boldsymbol{X} = \boldsymbol{P} + d \cdot \boldsymbol{l} \tag{B2}$$

where *d* is a scalar representing the distance of the segment between **P** and **X** that is obtained as follows:

$$d = -\sum_{i=1}^{N} p_i \cdot l_i + \sqrt{\left(\sum_{i=1}^{N} p_i \cdot l_i\right)^2 - \sum_{i=1}^{N} p_i^2 + 1} \tag{B3}$$

Finally, once **X** is known, the value of spectral acceleration associated to **X** can be obtained as follows:

$$S_{aX} = S_{aP} + \frac{x1 - p1}{r1 - p1}(S_{aR} - S_{aP}) \ \cdot \tag{B4}$$